ACS Catalysis

pubs.acs.org/acscatalysis
Research Article

Tuning the Reconstruction of Metal−Organic Frameworks during the Oxygen Evolution Reaction

Xiaoxin Ma, Lena Schröck, Guanhui Gao, Qing Ai, Maider Zarrabeitia, Caiwu Liang, Mian Zahid Hussain, Rachit Khare, Kun-Ting Song, Daniel J. Zheng, Max Koch, Ifan E. L. Stephens, Shujin Hou, Yang Shao-Horn, Julien Warnan,* Aliaksandr S. Bandarenka,* and Roland A. Fischer*

Cite This: ACS Catal. 2024, 14, 15916−15926
Read Online

ACCESS | Metrics & More | Article Recommendations | Supporting Information

ABSTRACT: Recently, there has been growing interest in the conversion of metal−organic frameworks (MOFs) into metal-hydroxide catalysts for alkaline oxygen evolution reactions (OERs). While studies have shown that the initial OER performance of MOF-derived intermediates surpasses that of traditional metal-hydroxide catalysts, ongoing debates persist regarding these catalysts' durability and electrochemical stability. Moreover, the inevitable reorganization (aging) of MOF-derived catalysts from disordered to ordered phases, particularly those primarily composed of nickel oxyhydroxides, remains a topic of discussion. To address these issues, we propose a straightforward approach to mitigating MOF reconstruction and modulating aging in harsh alkaline environments by introducing additional organic carboxylate linkers into electrolytes. Specifically, we focus on two examples: Ni-BPDC-MOFs and NiFe-BPDC-MOFs, of formula $[M_2(OH)_2BPDC]$ (M: Ni and Fe; BPDC = 4,4′-biphenyldicarboxylate). Experimental results indicate that alkaline electrolytes containing additional BPDC linkers exhibit enhanced OER activity and a prolonged electrochemical lifespan. Complemented by in situ Raman spectroscopy, our findings suggest that manipulating the coordination equilibrium of the organic linker involved in Ni-MOF formation (linker assembly) and reconstruction (linker leaching) leads to the formation of more disordered nickel oxyhydroxide phases as the active catalyst material, which shows enhanced OER performance.

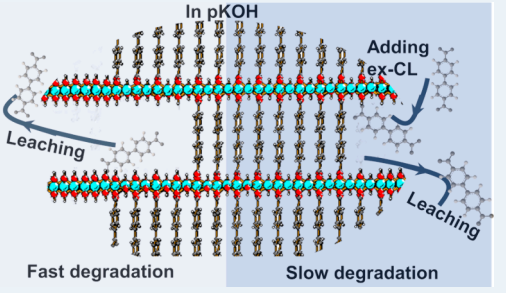

KEYWORDS: *metal−organic frameworks, oxygen evolution reactions, reconstruction, metal hydroxide, equilibrium*

INTRODUCTION

Selecting suitable electrocatalysts is crucial for advancing the oxygen evolution reaction (OER), a key step in hydrogen production.[1,2] Given the depletion of fossil fuels, finding alternatives is vital for the evolving energy landscape.[3,4] Since their inception, metal−organic frameworks (MOFs) have captured considerable attention as potential OER catalysts.[5−11] This recognition stems from their structural versatility,[12−16] the diverse array of metal nodes, and, notably, their demonstrated efficacy in reported OER applications.[17−21]

Following an in-depth discourse on the role of MOFs in alkaline OER, it has become apparent that many MOFs primarily function as precursors, i.e., as precatalysts to the active phase. When directly employed in OER applications, they undergo reconstruction, forming metal hydroxide or oxyhydroxide.[22,23] Substantial research has indicated that catalysts derived from MOFs in this way can exhibit superior activity compared to the closely related but conventional reference systems, particularly those featuring non-noble metals like Ni, Co, Fe, and Mn.[24−26] Moreover, when compared to noble metals, the non-noble electrocatalysts, especially prevalent Ni-based electrocatalysts, offer general advantages in terms of high abundance and low cost albeit often grappling with stability issues.[27,28] For instance, pristine $Ni(OH)_2$ struggles with the aging process in alkaline environments, transitioning from the disordered α-$Ni(OH)_2$ to the more ordered β-$Ni(OH)_2$ phase, resulting in a decline in OER activity.[29,30]

In a previous study, we explored an isoreticular series of $[Ni_2(OH)_2L]$ featuring carboxylate linkers of varying lengths that modulate the overall stability of the MOF in the electrolyte and during OER (L = linker = 1,4-benzendedicarboxylate, BDC; 2,6-napthalenedicarboxylate, NDC; 4,4′-biphenyldicarboxylate, BPDC; and 4,4″*p*-terphenyldicarboxylate, TPDC).[31] In this and related systems, it has been shown that the MOF will transfer to metal hydroxide first and then to oxyhydroxide during the OER process, but interestingly, the choice of the linker exerted control over the transformation of

Received: June 18, 2024
Revised: September 12, 2024
Accepted: September 25, 2024
Published: October 11, 2024

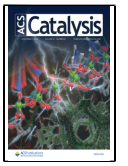

https://doi.org/10.1021/acscatal.4c03618
ACS Catal. 2024, 14, 15916−15926

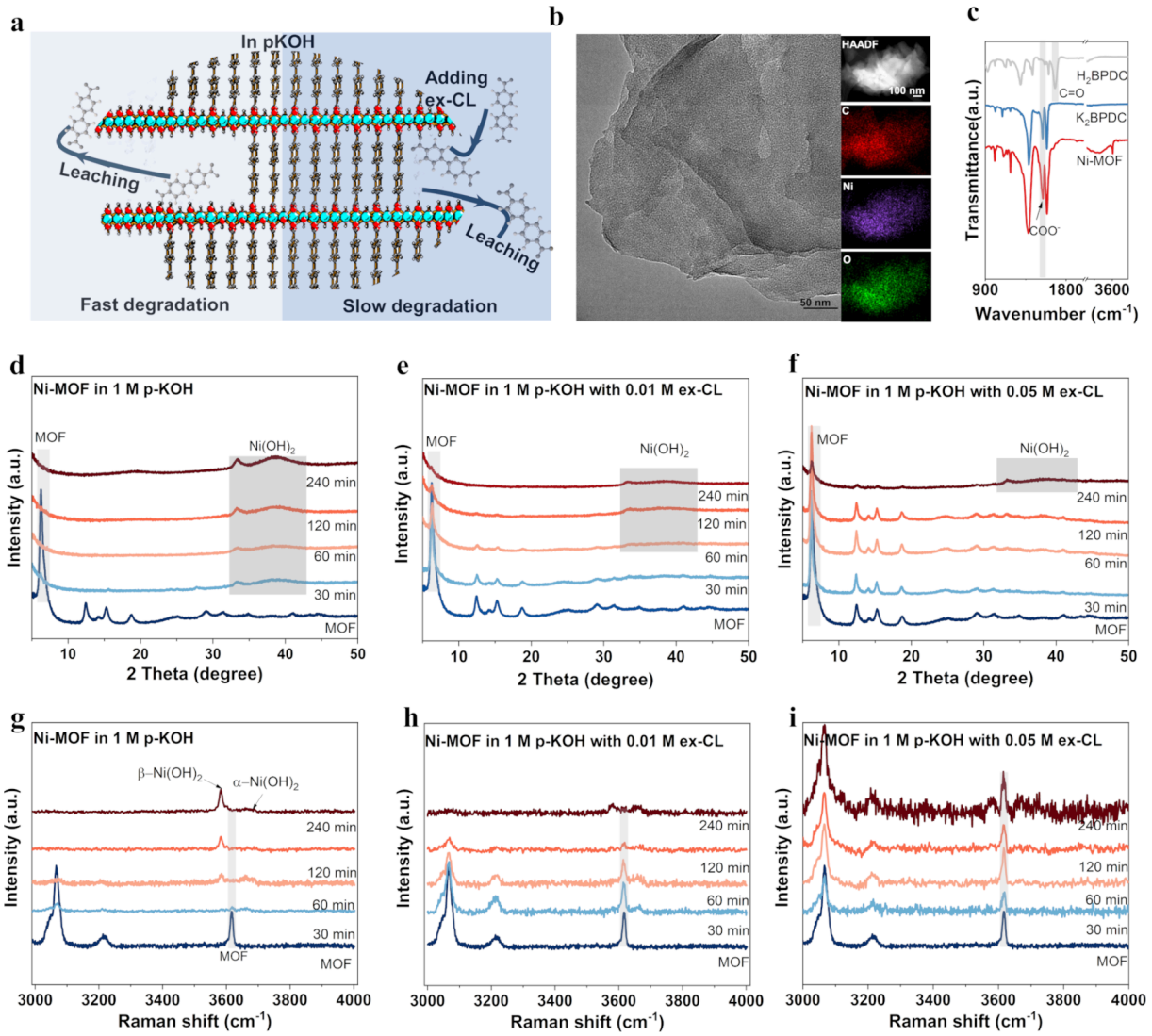

Figure 1. (a) Schematic illustration of the degradation process of Ni-MOF ($[Ni_2(OH)_2BPDC]$) in alkaline electrolytes with/without the extra carboxylate linker. (b) TEM and HAADF images of Ni-MOF along with the corresponding EDS elemental maps with Ni, O, and C. (c) FTIR of H_2BPDC, of the potassium linker salt K_2BPDC, and of the Ni-MOF. XRD pattern of time dependence for Ni-MOFs in 1 M purified KOH (p-KOH; Fe trace free) in the presence of various concentrations of K_2BPDC (extra-linker, ex-CL): (d) 0.00 M ex-CL (linker-free, similar to ref 31), (e) 0.01 M ex-CL, and (f) 0.05 M ex-CL. Time-dependent Raman spectra of Ni-MOFs in 1 M p-KOH in the presence of various concentrations of ex-CL: (g) 0.00 M ex-CL (linker-free), (h) 0.01 M ex-CL, and (i) 0.05 M ex-CL.

Ni-MOF, guiding it into distinct nickel hydroxide phases with a ratio depending on the type of linker chosen. The linker plays a pivotal role in affecting the MOF activation and decelerating the degradation and reconstruction processes, i.e., in modulating the reconstruction kinetics, resulting in tuning the OER activity. When considering the MOF reconstruction to the metal hydroxides as a chemical equilibrium, the process can take the form by

$$[Ni_2(OH)_2L](s) + 2OH^-(aq) \rightarrow 2Ni(OH)_2(s) + L^{2-}(aq);\ pK_R(L)\ (L:\ \text{Linker})$$

This assumption prompted a consideration: what if additional free linkers were introduced to the alkaline electrolyte? Would the equilibrium be shifted and the reconstruction reaction decelerate as the concentration of the available linker increases? How would that influence the OER performance of the system?

Motivated by this, we investigated the impact of introducing additional free linkers to a strong alkaline electrolyte during electrocatalysis, hypothesizing its potential to decelerate the reconstruction reaction, as shown in Figure 1a. We selected $[Ni_2(OH)_2BPDC]$ for a detailed evaluation and found that this system has prolonged stability, reduced reconstruction, and enhanced electrochemical lifetime with the introduction of the extra carboxylate linker (ex-CL = BPDC) in the electrolyte. Expanding this hypothesis to NiFe-MOFs as another case study revealed a similar behavior, although NiFe-MOFs displayed higher intrinsic instability and a tendency to transition into a more disordered phase with Fe assistance, compared to pure Ni-MOF systems.

RESULTS AND DISCUSSION

The Ni-MOF, with the formula $[Ni_2(OH)_2BPDC]$, was synthesized following our previous method,[31] revealing distinctive 2D morphologies with C, O, and Ni elements in

https://doi.org/10.1021/acscatal.4c03618
ACS Catal. 2024, 14, 15916−15926

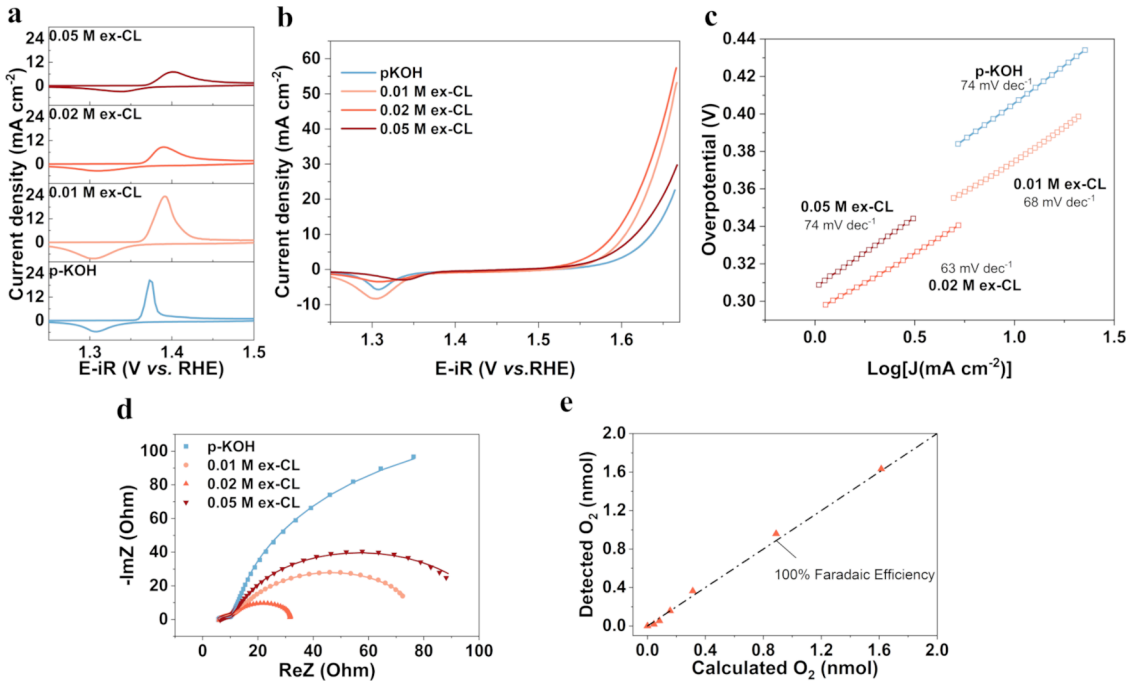

Figure 2. Electrochemical characterization of Ni-MOF in 1 M p-KOH with the addition of 0.00 0.05 M ex-CL. The Ni-MOFs were cycled (activation process) from 1.13 to 1.67 V vs. the RHE with IR correction at 10 mV/s (Hg/HgO was used as the experimental reference electrode, and potentials were corrected for RHE, glassy carbon (GC) as the RDE working electrode, Figure S7). The reported electrochemical data were taken when the intensity of anodic peaks of Ni^{3+}/Ni^{2+} no longer increased. (a) Redox peaks of $Ni^{2+/3+}$. (b) OER activity. (c) Tafel slope. (d) Electrochemical impedance spectroscopy (EIS) with the fitting line at 1.546 V vs. RHE. (e) Faradaic efficiency with 0.02 M ex-CL. All results given here are measured after the CV activation process (for details, see the SI).

Figure 1b. Atomic force microscopy (AFM) characterization confirmed this nanosheet structure with a thickness of under 10 nm (Figure S1). XANES analysis (Figure S2) verified the presence of Ni^{2+} and showcased a characteristic and sharp μ^3−OH band at ∼3611 cm^{-1} in the FTIR spectra (Figure 1c).

Following structural characterization, we further investigated the MOF's behavior under various electrolytes without applied potentials. Given the known sensitivity of the OER activity to pH changes and considering our previous findings on the impact of pH on MOF reconstruction, we used the potassium salt K_2BPDC (ex-CL) instead of H_2BPDC to avoid any significant changes in the pH upon addition of ex-CL to the electrolyte, as indicated in Table S1. As shown in Figure 1c, the ν(C═O) of the COOH species at 1679 cm^{-1} in H_2BPDC shifted to 1586 and 1543 cm^{-1} in the deprotonated COO^- species of K_2BPDC and Ni-BPDC-MOF, respectively.[32]

The powder X-ray diffraction (PXRD) patterns of Ni-MOF in Figure 1d revealed distinct characteristic reflections at 6.2°, signifying a metal−ligand−metal lattice spacing of around 14.2 nm.[31] These reflections began to degrade upon immersion in 1 M purified KOH (p-KOH) and vanished after 60 min. Concurrently, α/β-$Ni(OH)_2$ phases emerged at around 19, 33, and 38°, with their intensity increasing with prolonged exposure time.[33] In contrast, the introduction of the extra carboxylate linker (K_2BPDC, ex-CL) significantly enhanced the stability of the MOF as its reflection at 6.2° was still observed after 120 min of immersion in 1 M p-KOH with 0.01 M ex-CL (Figure 1e). Higher ex-CL concentrations improved the MOF's stability, with clear MOF reflections observed even after 240 min of treatment in 1 M p-KOH with 0.02 and 0.05 M ex-CL (Figures S3 and 1f). Interestingly, the $Ni(OH)_2$ reflections resulting from the MOF conversion exhibited significantly broader peaks in the presence of ex-CL, suggesting that more disordered phases were formed under these conditions.

Raman spectra in Figures 1g−i and S4−S6 provided detailed insights into the transformation process, quantifying derived $Ni(OH)_2$ phases during exposure in 1 M p-KOH with and without the addition of 0.01−0.05 M ex-CL. The characteristic bands of phenyl rings and carboxylate groups from Ni-MOF decreased with the increasing exposure time in 1 M p-KOH, with the appearance of new broad peaks centered at 311 (E_g) and 450 cm^{-1} (A_{1g}) for the $Ni(OH)_2$ phase, as shown in Figure S4.[29,33] Simultaneously, the μ^3−OH bridge signal for pristine Ni-MOF at 3617 cm^{-1} decreased, transforming into two new bands, assigned to β-$Ni(OH)_2$ at ∼3582 cm^{-1} and α-$Ni(OH)_2$ at around ∼3673 cm^{-1} (Figure 1g).[34] After 240 min of exposure in 1 M p-KOH, the β-$Ni(OH)_2$ band was 6.15 times stronger than α-$Ni(OH)_2$. In contrast, the addition of ex-CL slowed down the aging process from the disordered α-$Ni(OH)_2$ to the ordered β-$Ni(OH)_2$ (Figures S5, S6 and 1h−i), while the phenyl ring bands at 1603 cm^{-1}, which are characteristic of the MOF, remained prominent.[35] Specifically, for the Ni-MOF in 0.01 M ex-CL in p-KOH after 60 min, the Raman band at 3673 cm^{-1} assigned to α-$Ni(OH)_2$ was now stronger than β-$Ni(OH)_2$. After 240 min, the ratio β-$Ni(OH)_2$:α-$Ni(OH)_2$ was 1.2 for Ni-MOF in 0.01 M ex-CL in p-KOH and 0.94 and 0.88 for Ni-MOF in 0.02 and 0.05 M ex-CL in p-KOH, respectively.

In summary, the presence of an additional linker resulted in a significant decrease in the β/α phase of $Ni(OH)_2$. By combining the time-dependent XRD and Raman findings discussed above, we affirm the validity of our hypothesis, demonstrating a discernible influence of the extra carboxylate

https://doi.org/10.1021/acscatal.4c03618
ACS Catal. 2024, 14, 15916−15926

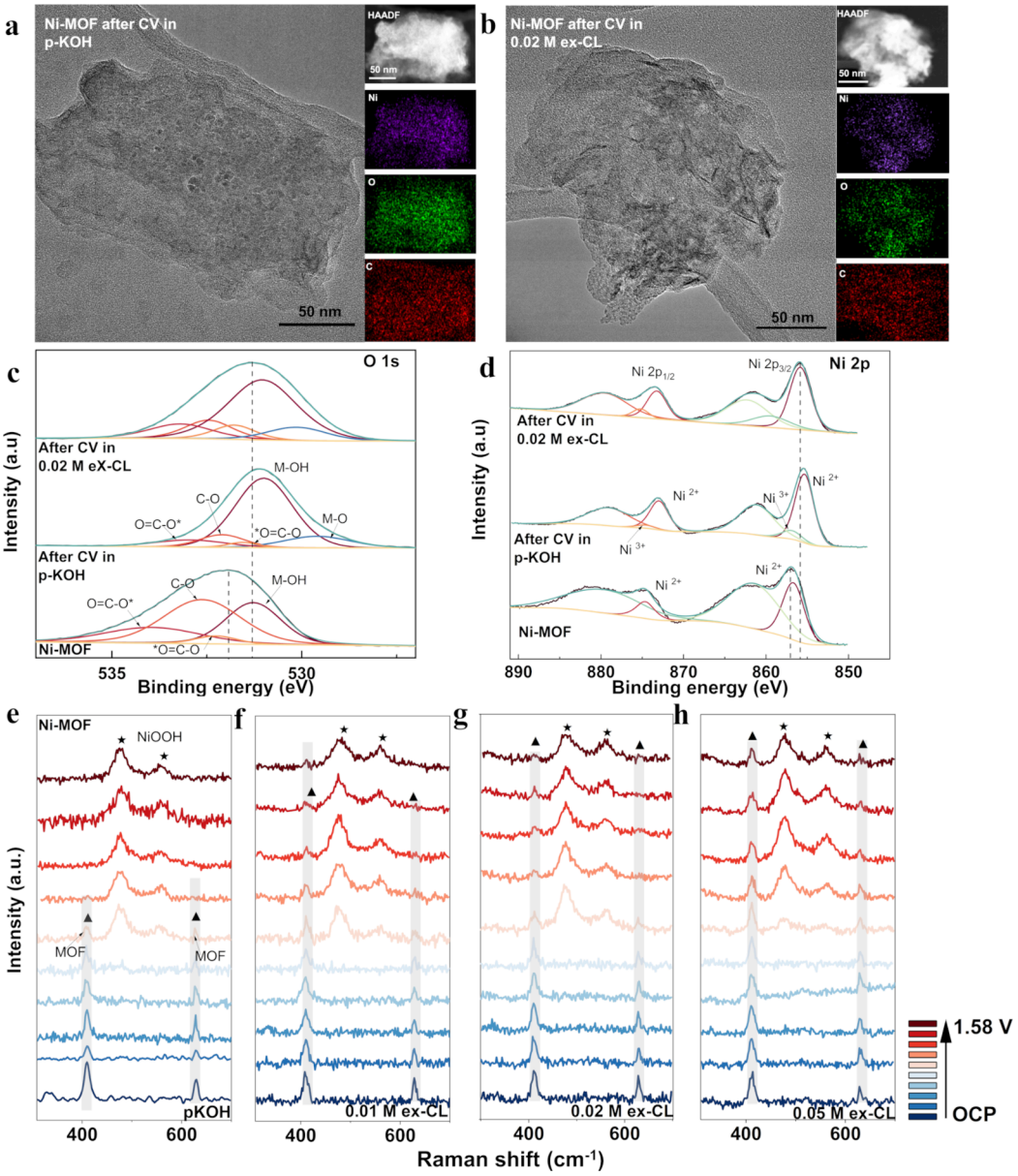

Figure 3. TEM and HAADF images along with the corresponding EDS elemental mapping of Ni-MOF measured ex situ after 30 cycles of CV (1.13−1.67 V vs. the RHE, 10 mV s^{-1}) in (a) 1 M p-KOH and (b) 1 M p-KOH with 0.02 M ex-CL. Corresponding XPS spectra of (c) O 1s and (d) Ni 2p photoelectrons. In situ Raman spectra of Ni-MOF around 300−700 cm^{-1}, a range diagnostic for distinguishing Ni-MOF from NiOOH species, were recorded in a homemade electrochemical cell in 1 M p-KOH with (e) 0.00 M ex-CL (linker-free), (f) 0.01 M ex-CL, (g) 0.02 M ex-CL, and (h) 0.05 M ex-CL, ranging from open circuit potential (OCP) to 1.58 V vs RHE (with OCP, 1.03, 1.13, 1.23, 1.33, 1.38, 1.43, 1.48, 1.53, 1.58 V vs. RHE). A quartz substrate coated with Au of 0.785 cm^{-2} was used as the working electrode for the in situ Raman test, Hg/HgO as the reference electrode, and Pt wire as the counter electrode. All potentials have been corrected to RHE. In Figure 3e−h, the symbol ▲ represents the MOF peak and the symbol ★ represents NiOOH.

linker on the reconstruction of Ni-MOF, the improved stability of the Ni-MOF in the alkaline environment, and the inhibition of the aging process in the derived $Ni(OH)_2$.

Shifting our focus to extra-linkers' influence on electrochemistry, Ni-MOF (48 μg) deposition on GC was carried out using a standard drop-casting method (ink preparation and method details are available in the SI). Throughout this work, unless specified otherwise, GC serves as the working electrode. Cyclic voltammograms (CVs) were executed in alkaline electrolytes (1 M p-KOH with [ex-CL] = 0.00−0.05 M) from 1.13 to 1.67 V vs. RHE with IR correction (GC as the RDE working electrode, and Hg/HgO as the experimental reference electrode, with potentials corrected for RHE, Figure S7) and a scan speed of 10 mV/s, as visualized in Figures S8 and S9. The redox peaks of Ni^{3+}/Ni^{2+} in Ni-MOF display an ascending pattern starting from the first cycle in 1 M p-KOH (Figure S8a), indicating the degradation and subsequent reconstruction of Ni-MOF into $Ni(OH)_2$/NiOOH.

Furthermore, the OER activity was assessed after the intensity of the anodic peaks did not increase, as depicted in Figure 2a,b. The oxidation peaks of Ni^{3+}/Ni^{2+} exhibited a slight positive (anodic) shift with the introduction of ex-CL, transitioning from 1.37 (in p-KOH) to 1.39 (with 0.01 and 0.02 M ex-CL), and to 1.40 V vs. RHE (with 0.05 M ex-CL). The overpotential at 10 mA cm^{-2}, indicative of the OER activity, decreased from 404 ± 11 mV in 1 M p-KOH to 375 ±

https://doi.org/10.1021/acscatal.4c03618
ACS Catal. 2024, 14, 15916−15926

4 and 355 ± 7 mV with 0.01 and 0.02 M ex-CL, respectively. However, it increased to 363 ± 6, 371 ± 3, and 380 ± 13 mV for 0.03, 0.04, and 0.05 M ex-CL, respectively (Figures 2b and S10). Correspondingly, the Tafel slope (Figure 2c) was calculated to 74, 68, 63, and 74 mV dec^{-1} with 0.00, 0.01, 0.02, and 0.05 M ex-CL, respectively, highlighting the enhanced OER kinetics for Ni-MOFs in an alkaline environment in the presence of extra carboxylate linkers. Moreover, the turnover frequencies (TOFs) were calculated using two methods: inductively coupled plasma atomic emission spectroscopy (ICP-OES) measurements of Ni in the MOF-coated electrodes and the integration of the oxidation peak in the OER in Figure S11. These methods determined the number of moles of Ni deposited on the GC electrode and the molar amount of electrochemically accessible Ni reacted during the CV activation process, respectively. The ex-CL addition yielded higher TOF values compared to the linker-free electrolyte, with the highest values observed at 0.02 M ex-CL with 0.11 and 0.40 s^{-1} for Ni, based on ICP-OES and the $Ni^{2+/3+}$ oxidation peak integration as the lower and upper limits, respectively, for TOF.

Figure S12 displays the EIS results within a potential range from 1.466 to 1.586 V vs RHE. The adsorption resistances (R_a) of Ni-MOF with various electrolytes were compared to the values obtained under 1.546 V vs RHE using an equivalent electric circuit model, as depicted in Figures 2d and S13. Compared with the negligible difference of the resistance of the electrolyte (R_s) in different electrolytes in Figure S14, the R_a drops as the ex-CL increases to 0.01−0.02 M, indicating easier formation of the active intermediates γ-NiOOH from α-$Ni(OH)_2$, potentially contributing to their higher activity.[36]

To delve deeper into the electrochemical implications of the extra-linker in the electrolytes, we used a reference β-$Ni(OH)_2$ bulk sample, which avoids the original phase influence based on the Bode scheme and the self-linkers' interference from MOFs. This reference catalyst was compared with the Ni-MOFs' OER behavior in alkaline conditions selecting extra-linker-free conditions and 0.01 M ex-CL addition in p-KOH (Figure S15). The very similar activities of these reference systems indicate that the effect of ex-CL on a $Ni(OH)_2$/NiOOH catalyst's surface, e.g., adsorption and modulating the active sites, can be considered negligible also in our case of the Ni-MOF-derived catalyst materials.[37] Rather, it implies that the observed effect of ex-CL on the OER in our case relates to the intrinsic kinetics of Ni-MOF reconstruction and the phase ratio of the derived NiOOH.

Moreover, the electrochemical stability of ex-CL under the conditions of our experiments was carefully verified to avoid misinterpretations. Specially, activated β-$Ni(OH)_2$ reference catalysts on GC were exposed to constant potentials of 1.6−2.3 V vs. RHE (1.6, 1.8, and 2.3 V) for 20 min (for each potential) in a neutral solution containing 0.05 M ex-CL (the choice of the neutral solution is to avoid the interference of the alkali for HPLC; details as shown in the SI). After the electrochemical measurements, each electrolyte solution underwent HPLC analysis, revealing no traces of degradation products of the carboxylate linkers, such as biphenyl (Table S2).[38] Additionally, the pristine GC electrode was tested in the linker-free 1 M p-KOH and with 0.02 M ex-CL, and no remarkable changes were found (Figure S16). Finally, the Faradaic efficiency was measured to be 103 ± 2.4% for our Ni-MOF-derived OER catalyst tested in 0.02 M ex-CL (Figure 2e). Combining these results with the unchanged NMR results of the electrolytes before and after CV (Figure S17), it is suggested that the oxidation of the carboxylate linker here, for example, involving possible decarboxylation and biphenyl formation, could be ignored.[39]

As is common, the presence of Fe in alkaline electrolytes significantly enhances the performance of Ni-based catalysts in OER applications.[40] To investigate potential contamination, elemental mappings using electron diffraction spectroscopy (EDS) in the transmission electron microscopy (TEM) mode were conducted on Ni-MOF samples after 30 cycles of CV (1.13−1.67 V vs. the RHE, 10 mV/s) in both 1 M p-KOH (Fe-free) and with the addition of 0.02 M ex-CL. No Fe was detected in Figure 3a,b. Furthermore, ICP-OES (Figure S18) results indicated that the as-prepared K_2BPDC salt contained a low trace concentration of Fe (0.025 ppm), suggesting that trace-level Fe contamination is not responsible for the observed enhancement in the OER activity with alkaline electrolytes containing extra carboxylate linkers.[29]

Additionally, Ni-MOF-derived electrodes operated in different electrolytes were investigated post OER experiments. In Figure S19, ex situ high-resolution transmission electron microscopy (HRTEM) analysis revealed clear lattice fringes with spacings of approximately 0.20 and 0.24 nm, corresponding to the (101) planes of the NiO phase and the (002) planes of NiOOH, respectively.[41] These findings confirm the reconstruction process during the OER for both Ni-MOF samples in linker-free alkaline electrolytes and those with 0.02 M ex-CL. Furthermore, ex situ X-ray photoelectron spectroscopy (XPS) analysis was performed to investigate changes in the surface chemical states of the cycled electrodes. In Figure 3c, the O 1s spectrum of pristine Ni-MOF exhibited four components at approximately 533.9, 532.6, 532.3, and 531.3 eV, corresponding to O═C−O* (oxygen bonded to a single bond to a carbonyl group), C−O (ether group), *O═C−O (oxygen bonded to a double bond to the carbonate), and Ni−OH bonds, respectively.[42] The intensities of the carbonaceous species (C−O and O═C−O) notably decreased after electrochemical activation, suggesting leaching of the carboxylate linker.

For the cycled Ni-MOF-derived electrodes, an additional peak at lower binding energies (529.6 eV) was observed in both electrolytes, likely attributable to the Ni-oxide (Ni−O) species. It should be noted that the Ni-MOFs showed insulating character during the XPS experiment, which was mitigated by the use of an electron gun. However, small charging effects were still observed. The Ni 2p spectrum of pristine MOFs shows multiplet splitting and satellite peaks that were centered at binding energies of about 856.9 (Ni $2p_{3/2}$) and 874.8 eV (Ni $2p_{1/2}$) in Figure 3d, which is assigned to the oxidation state Ni^{2+}, in line with the results from XANES (Figure S2). Meanwhile, the Ni $2p_{3/2}$ spectra of the cycled electrodes revealed two distinct peaks: $Ni(OH)_2$/NiO and Ni^{3+}, due to NiOOH formation. A negative shift of the Ni 2p peaks to lower binding energies after cycling in both electrolytes suggests an altered local electronic structure of the Ni atom on the surface due to the gradual leaching of the carboxylate linkers, particularly due to the formation of NiO-like moieties, confirmed by HRTEM patterns, which typically exhibits a lower binding energy than $Ni(OH)_2$ and Ni-MOF.[43]

In situ Raman spectroscopy was also employed to systematically explore the impact of structural reconstruction during OER with the addition of ex-CL, as illustrated in Figures 3e−h and S20−S22. When the Ni-MOF was tested in

https://doi.org/10.1021/acscatal.4c03618
ACS Catal. 2024, 14, 15916−15926

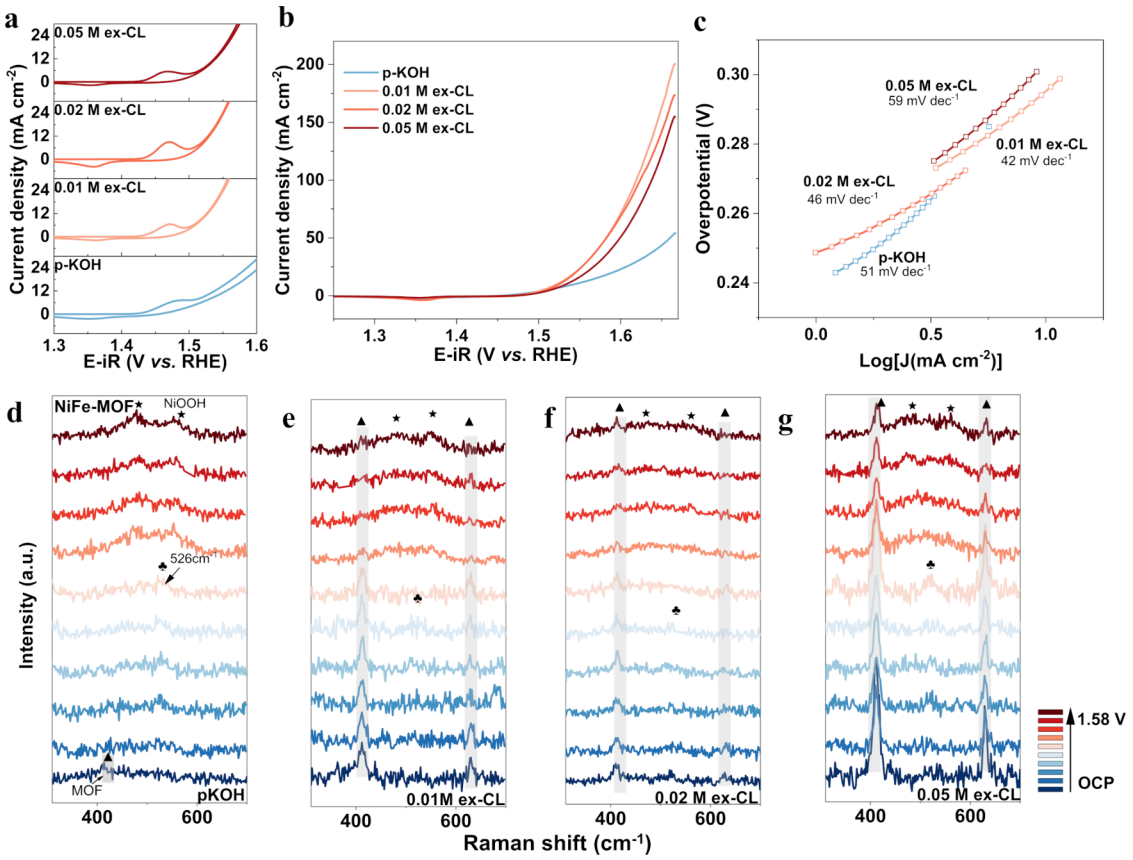

Figure 4. Electrochemical characterization of NiFe-MOF in 1 M p-KOH with the addition of 0.00−0.05 M ex-CL. The NiFe-MOFs were cycled (activation process) from 1.13 to 1.67 V vs. the RHE with IR correction with 10 mV/s (Hg/HgO was used as the experimental reference electrode, and potentials were corrected for RHE, GC as the RDE working electrode). The reported electrochemical data were taken when the intensity of anodic peaks of Ni^{3+}/Ni^{2+} no longer increased: (a) redox peaks of NiFe-MOF ($[(NiFe)_2(OH)_2BPDC]$) in 1 M p-KOH with 0.00−0.05 M ex-CL. (b) OER activity; (c) Tafel slope in 1 M P-KOH with 0.00−0.05 M ex-CL. In situ Raman spectra in 1 M p-KOH with (d) 0.00 M ex-CL (linker-free), (e) 0.01 M ex-CL, (f) 0.02 M ex-CL, and (g) 0.05 M ex-CL, ranging from OCP to 1.58 V vs. RHE (with OCP, 1.03,1.13,1.23,1.33,1.38, 1.43,1.48,1.53, 1.58 V vs RHE). In Figure 4d−g, the symbol ▲ represents the MOF peak, the symbol ★ represents NiOOH, and the symbol ♣ represents $NiFe(OH)_2$.

ex-CL free p-KOH (Figure 3e), two distinct bands at 407 and 629 cm^{-1} emerged at the OCP, originating from the framework incorporated linker of the Ni-MOF (Figure S23). Specifically, the 407 cm^{-1} band corresponds to out-of-plane skeletal vibrations, while the 629 cm^{-1} band corresponds to the ring deformation of the linker.[44] These characteristic MOF bands remained unchanged until the potential was raised to 1.38 V vs. RHE. Subsequently, two new Raman bands emerged around 479 cm^{-1} (Eg bending) and 560 cm^{-1} (A1g stretching), attributed to Ni−O vibrations of the surface intermediate NiOOH, concomitant with a decrease in the MOF band intensity.[45] Upon applying higher potentials in 1 M p-KOH, the MOF bands degraded and disappeared at 1.48 V. Notably, the MOF bands persisted longer with the additional ex-CL, seen in Figure 3f−h; particularly, a prominent band at 407 cm^{-1} of the MOF can still be observed even at 1.58 V *vs.* RHE in p-KOH with 0.05 M ex-CL. Interestingly, the presence of the coordinated COO^- species at 1429 cm^{-1} in the Ni-MOF decreased as the potential increased in Figures S20−S22. However, the presence of free (uncoordinated) COO^- at 1390 cm^{-1}, which resulted from the addition of ex-CL, remained clearly visible. The intensity ratio of the two Ni−O Raman bands (I_{560}/I_{479}) serves as a metric for evaluating the structural disorder/defect of the derived NiOOH. Specifically, a higher I_{560}/I_{479} ratio indicates a more disordered phase.[46] In 1 M p-KOH, the ratio of I_{560}/I_{479} reached 0.41 at 1.58 V vs RHE, significantly lower than the ratios observed in the presence of ex-CL, i.e., 0.77, 0.79, and 0.64 in 0.01, 0.02, and 0.05 M ex-CL, respectively. These results indicate that the additional ex-CL in the electrolyte induces a more disordered intermediate than that in the normal (pure) alkaline solution. Given that the O−H group between 3000 and 4000 cm^{-1} was masked by a significant water band during in situ Raman testing, our study combines in situ findings with time-dependent Raman results that track O−H changes and MOF degradation observed in XRD results. This supports the hypothesis that the use of an additional carboxylate linker can effectively modulate the dynamic equilibrium between the degradation and reconstruction of Ni-MOF precursors, leading to a highly OER-active intermediate $Ni(OH)_2/NiOOH$ species. Interestingly, this allows for the more disordered and, thus, more OER-active phase to be more abundant.

Furthermore, the mixed metal (solid solution) NiFe-MOF ($[(NiFe)_2(OH)_2BPDC]$) was used as another example (unless otherwise mentioned, the Ni:Fe ratio in this work is around 3:1, Figure S24) to further investigate the validity and scope of our hypothesis. Despite similarities in morphology and structure between the two isostructural MOFs (Figures S25−S28), the NiFe-MOF exhibited rapid degradation in alkaline electrolytes. Specifically, the characteristic MOF peak at 6.2°

https://doi.org/10.1021/acscatal.4c03618
ACS Catal. 2024, 14, 15916−15926

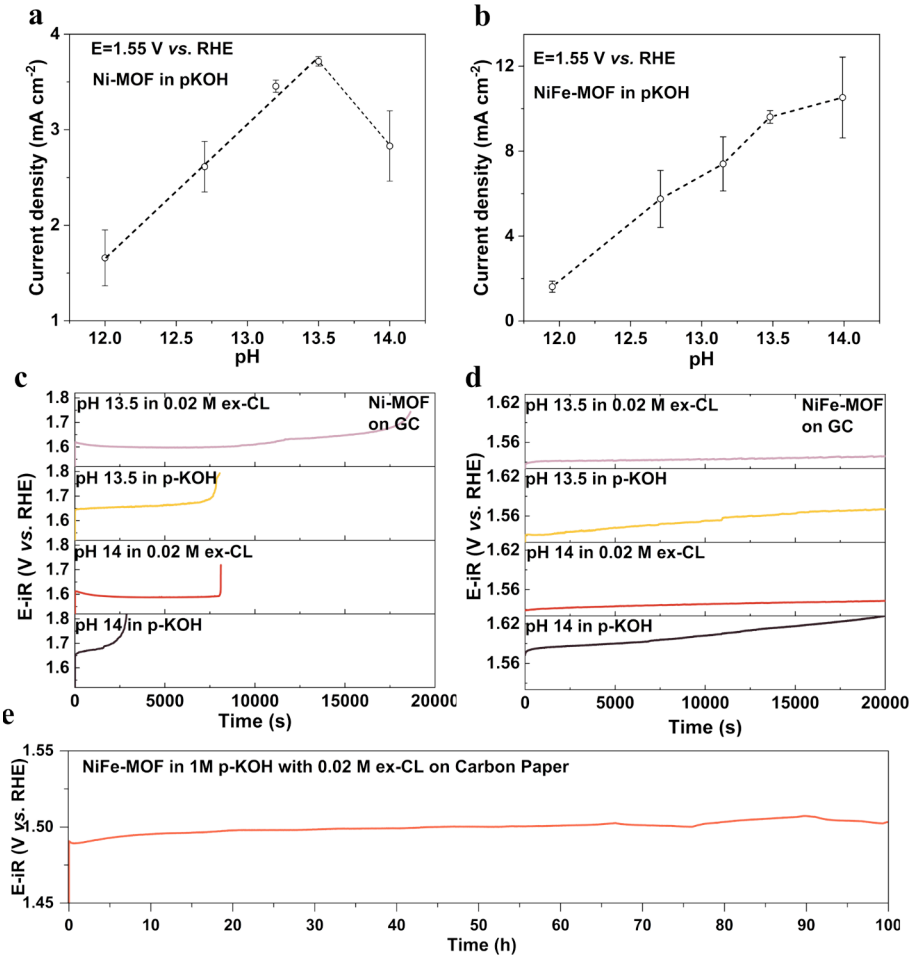

Figure 5. pH effect of (a) Ni-MOF and (b) NiFe-MOF in Fe-free p-KOH with pH 12.0−14.0. Chronopotentiometric response of (c) Ni-MOF and (d) NiFe-MOF on the glassy carbon (RDE) in p-KOH with pH 14.0 and pH 13.5, with and without ex-CL under current density at 10 mA cm^{-2}. (e) Chronopotentiometric response of NiFe-MOF in 1 M p-KOH (pH:14) with 0.02 M ex-CL using carbon paper as the collector under current density at 10 mA cm^{-2}.

(001) vanished completely within 30 min in 1 M p-KOH, with new peaks attributed to $NiFe(OH)_2$ emerging at 11, 23, 34, and 38° in Figures S29 and S30.[47] Furthermore, Raman data of NiFe-MOF submerged in p-KOH for 30 min unveiled additional bands at ∼453 and ∼526 cm^{-1}, indicative of the emergence of Ni−OH symmetric stretching mode vibrations and structural defects originating from $NiFe(OH)_2$ (Figures S31 and S32).[48] Adding extra linkers in the solution barely reduced the degradation of the MOF structure, as no discernible MOF peaks were detected after 30 min. However, analysis of the transformation process revealed that the resulting $NiFe(OH)_2$ compound exhibited increased disorder in solutions containing the extra-linker, as illustrated in Figure S33.

Electrochemical measurement of NiFe-MOF, following the same activation procedure as the Ni-MOF, yielded interesting insights (Figures 4a−c, S34, and S35). While the anodic peak remained relatively consistent across different conditions, the introduction of extra linkers resulted in improved OER activities. The overpotentials for 0.01, 0.02, and 0.05 M ex-CL were 295 ± 8, 291 ± 4, and 296 ± 9 mV, respectively, compared to the 313 ± 4 mV overpotential of 1 M p-KOH at 10 mA cm^{-2} in Figures 4b and S36. Tafel slope analysis further supported this trend with values of 51, 42, 46, and 59 mV dec^{-1} for concentrations increasing from 0.00 to 0.05 M ex-CL.

Furthermore, HRTEM images of cycles NiFe-MOFs in both ex-CL free p-KOH and with an additional linker concentration of 0.02 M revealed distinct lattice fringes corresponding to the (002) planes from NiOOH (or NiFeOOH) (Figures S37 and S38).[49] Additionally, EDS mapping confirmed the even distribution of Ni, Fe, and residual C (Figures S37 and S38). Analysis indicated a transition process during the OER, supported by supplementary XPS data showing a decrease in carbonaceous species, such as C−O and O═C−O (O═C−O* and *O═C−O), and an increase of M−O (Ni/Fe) oxides (Figure S39a). Notably, the Ni 2p spectrum of the pristine NiFe-MOFs resembled those of Ni^{2+} in the original Ni-MOF, with binding energies around 856.9 and 874.8 eV (Figure S39b). Postcycling electrodes exhibited the formation of Ni^{3+} species that were discernible from XPS deconvolution. Meanwhile, the Fe 2p region in the XPS indicates that the Fe oxidation state (Fe^{3+}) remains constant during cycling, which is in agreement with XANES analyses (Figures S39c and S40).

In situ Raman spectroscopy provided additional insights into electrochemical changes (Figure 4d−g). In a 1 M p-KOH solution, NiFe-MOF underwent a rapid transformation with MOF bands at 407 and 629 cm^{-1} to $NiFe(OH)_2$ at 526 cm^{-1} at the OCP, and the MOF bands completely disappeared at 1.03 V vs. RHE. Subsequently, the NiOOH peak appeared

https://doi.org/10.1021/acscatal.4c03618
ACS Catal. 2024, 14, 15916−15926

after 1.43 V vs. RHE. Interestingly, the synergy with Fe during reconstruction may induce a transition to a more disordered phase as compared to the process observed with Ni-MOF in p-KOH (1M). Beyond 1.58 V vs. RHE, the relative ratio of I_{560} /I_{479} increased to 0.59, significantly higher than that of Ni-MOF. Remarkably, the addition of ex-CL decelerated degradation, allowing MOF peaks to persist longer, as evidenced by peaks retained at 1.43 V vs. RHE for 0.01 M ex-CL and 1.58 V vs. RHE for 0.02 M ex-CL and 0.05 M ex-CL. The corresponding I_{560} /I_{479} ratios increased to 1.05, 1.12, and 1.02 for 0.01, 0.02, and 0.05 M ex-CL, respectively. In conclusion, although the presence of Fe renders NiFe-MOF significantly less stable in 1 M p-KOH solution, the resulting $NiFe(OH)_2$ primarily adopts a disordered α-$Ni(OH)_2$ phase. Despite rapid NiFe-MOF transformations, the addition of ex-CL to the electrolyte may induce a transition to a more amorphous, disordered phase, ultimately enhancing OER efficiency.

Additionally, another type of MOF, such as Ni-BDC-MOF (BDC: terephthalic acid), was explored in 1 M p-KOH with extra linkers (e.g., ex-CL-BDC, K_2BDC) to assess the general applicability of this approach to other MOF systems, as shown in Figure S41. Ni-BDC-MOF powders were first immersed in 1 M p-KOH, with and without additional carboxylate linkers (K_2BDC, ex-CL-BDC), for 15 min to investigate the degradation and reconstruction processes (Figure S41a). Compared to BPDC-MOFs, Ni-BDC-MOFs exhibited greater instability, with their characteristic MOF peaks disappearing completely and being replaced by the $Ni(OH)_2$ phase in all samples, even with the addition of ex-CL-BDC (0.00−0.10 M). The XRD patterns of Ni-BDC-MOF in 0.01 M ex-CL closely resembled those in pure KOH, indicating a similar reconstruction behavior. However, increasing ex-CL-BDC concentrations (e.g., 0.05 and 0.10 M) resulted in broader $Ni(OH)_2$ peaks, suggesting a more disordered structure at higher concentrations.

The OER activities of Ni-BDC-MOF in alkaline electrolytes with varying ex-CL-BDC concentrations (0.00−0.10 M) were further examined, as shown in Figure S41b. Significant improvements in the OER performance were observed at 0.10 and 0.05 M ex-CL-BDC, with overpotentials of 392 and 423 mV, respectively, which were substantially lower than the 468 mV measured in pure KOH. Thus, beyond BPDC-MOFs, this strategy of adding extra carboxylate linkers also proves effective in modifying the surface reconstruction process in BDC-type MOFs (Ni), despite their inherent instability in alkaline electrolytes.

Prior to conducting chronopotentiometry experiments, the influence of pH on MOF degradation and reconstruction was explored (Figures S42 and S43). Ni-MOF in this work exhibited high stability at pH levels of 11 and 13, with only a small amount of α-$Ni(OH)_2$ formation observed after immersion in a 0.1 M p-KOH solution with a pH of 13.2 for 240 min. NiFe-MOF degradation was somewhat inhibited, with distinct MOF bands still visible after immersion in solutions with pH levels of 11 for 240 min and 13.2 for 30 min. Nevertheless, the pH level affects the reconstruction process. This is supported by data showing a correlation between lower pH levels and more disorder in the resultant $NiFe(OH)_2$. Additionally, the amount of β-$Ni(OH)_2$ phase, estimated from the ν(OH) Raman peak at ∼3580 cm^{-1}, is reduced when the pH is lower. For example, the amount of β-$Ni(OH)_2$ after 240 min at a pH of 13.2 was lower compared to that at pH 14.

Upon MOF activation in various pH electrolytes until reaching a stable state, the OER performance was evaluated (Figures 5a,b and S44). Surprisingly, the impact of pH on the current density of Ni-MOFs does not follow a linear trend but exhibits a volcano-like pattern, with the maximum current density observed at pH 13.5 (0.5 M p-KOH) at 1.55 V vs. RHE. NiFe-MOF exhibits a more linear behavior across all pH levels; however, the slope between pH 14 and 13.5 is less steep than between pH 13.5 and 12. These results suggest that OER activity is reliant on pH level as the precursor MOF to the active phases is significantly influenced by the pH. Consequently, chronopotentiometry analysis of Ni/NiFe-MOF was conducted not only in a pure solution or an extra-linker solution (0.02 M ex-CL) but also at varying pH levels, specifically pH 13.5 and 14.

Figure 5c illustrates the electrochemical durability of Ni-MOF deposited on a GC electrode at a current density of 10 mA cm^{-2}. The data indicate that a decrease in the pH positively influences the electrochemical stability. For instance, Ni-MOF tested in a 0.5 M p-KOH solution with a pH of 13.5 can maintain activity for about 2 h under a current density of 10 mA cm^{-2}, whereas under comparable conditions but with a pH of 14, deactivation takes place in less than 1 h. The introduction of the additional linker to the electrolytes extends the duration, under a current density of 10 mA cm^{-2}, approximately to 2.24 h in a 1 M p-KOH solution with pH 14 using a concentration of 0.02 M ex-CL. In a 0.5 M p-KOH solution (pH 13.5), the duration extends to about 5.2 h for Ni-MOF with the same concentration of ex-CL. Importantly, the presence of Fe enhances the electrochemical stability at a current density of 10 mA cm^{-2}. NiFe-MOF remains active even in highly alkaline solutions of 1 M p-KOH for a duration of 5.5 h, with degradation rates of 3.2 and 2.6% observed for 0.5 M p-KOH in Figure 5d. Upon the addition of 0.02 M ex-CL, the system exhibits increased stability, with the potential almost constant and experiencing mere 0.9 and 0.7% increases at pH 14 and pH 13.5, respectively. Considering the limitations on the GC substrate, NiFe-MOF was also applied to carbon paper to assess chronopotentiometry at a current density of 10 mA cm^{-2} in a 1 M p-KOH solution with 0.02 M ex-CL as shown in Figure 5e. Even after 100 h, electrochemical stability remained satisfactory. These findings from electrochemical stability tests and pH impact demonstrate that modulating the reconstruction process of MOFs toward the more disordered active metal-hydroxide phases can enhance activities related to OER and can improve long-term electrochemical performance.

CONCLUSIONS

During the OER process, (Fe)Ni-MOFs undergo reconstruction in the alkaline environment, transitioning from MOF precursors to metal hydroxides and eventually oxyhydroxides, which serve as active species. In this study, we manipulated the underlying MOF reconstruction process by employing a coordination modulation strategy. This strategy involved introducing additional carboxylate ligands to shift the coordination equilibrium at the metal sites, thereby competing with hydroxide ions, water, and other ligands. Time-resolved analyses using PXRD and Raman spectroscopies revealed that the presence of extra carboxylate linkers slows the reconstruction of the MOFs without applied potentials. Moreover, increasing the concentration of linkers in alkaline solutions prolongs the preservation of the bulk MOF structure

https://doi.org/10.1021/acscatal.4c03618
ACS Catal. 2024, 14, 15916−15926

after alkali treatment. This influences the reconstruction process, also delaying the transition from a disordered to an ordered metal-hydroxide phase. In situ Raman spectroscopy during the OER demonstrates that this reconstruction process is the primary factor contributing to the observed increase in the level of OER activity. The introduction of extra linkers extends the electrochemical lifetime in harsh alkaline environments by modifying the phase composition toward the more disordered and more active metal oxyhydroxide phase, which becomes more abundant. These results provide new insights into improving the electrochemical performance of derived materials as OER catalysts in alkaline electrolytes, offering a deeper understanding of their electrocatalytic mechanisms.

■ ASSOCIATED CONTENT

Supporting Information

The Supporting Information is available free of charge at https://pubs.acs.org/doi/10.1021/acscatal.4c03618.

Experimental Section and characterization details, HRTEM and AFM images, XRD patterns, Raman spectroscopy, XANES, and XPS data, ICP-OES data, CVs, TOF, NMR, and HPLC results (PDF)

■ AUTHOR INFORMATION

Corresponding Authors

Julien Warnan − *Chair of Inorganic and Metal−Organic Chemistry, Department of Chemistry, TUM School of Natural Sciences, Technical University of Munich, 85748 Garching, Germany; Catalysis Research Center, Technical University of Munich, 85748 Garching, Germany;* orcid.org/0000-0003-2729-8997; Email: julien.warnan@tum.de

Aliaksandr S. Bandarenka − *Physics of Energy Conversion and Storage, Department of Physics, TUM School of Natural Sciences, Technical University of Munich, 85748 Garching, Germany; Catalysis Research Center, Technical University of Munich, 85748 Garching, Germany;* orcid.org/0000-0002-5970-4315; Email: bandarenka@ph.tum.de

Roland A. Fischer − *Chair of Inorganic and Metal−Organic Chemistry, Department of Chemistry, TUM School of Natural Sciences, Technical University of Munich, 85748 Garching, Germany; Catalysis Research Center, Technical University of Munich, 85748 Garching, Germany;* orcid.org/0000-0002-7532-5286; Email: roland.fischer@tum.de

Authors

Xiaoxin Ma − *Chair of Inorganic and Metal−Organic Chemistry, Department of Chemistry, TUM School of Natural Sciences, Technical University of Munich, 85748 Garching, Germany; Physics of Energy Conversion and Storage, Department of Physics, TUM School of Natural Sciences, Technical University of Munich, 85748 Garching, Germany*

Lena Schröck − *Chair of Inorganic and Metal−Organic Chemistry, Department of Chemistry, TUM School of Natural Sciences, Technical University of Munich, 85748 Garching, Germany*

Guanhui Gao − *Department of Materials Science and Nano Engineering, Rice University, Houston, Texas 77005, United States; Electron Microscopy Core at the Division of Research, University of Houston, Houston, Texas 77204, United States*

Qing Ai − *Department of Materials Science and Nano Engineering, Rice University, Houston, Texas 77005, United States*

Maider Zarrabeitia − *Helmholtz Institute Ulm (HIU), D-89081 Ulm, Germany; Karlsruhe Institute of Technology (KIT), D-76021 Karlsruhe, Germany*

Caiwu Liang − *Department of Materials, Imperial College London, London SW7, U.K.*

Mian Zahid Hussain − *Chair of Inorganic and Metal−Organic Chemistry, Department of Chemistry, TUM School of Natural Sciences, Technical University of Munich, 85748 Garching, Germany;* orcid.org/0000-0003-3307-5925

Rachit Khare − *Chair of Technical Chemistry II, Department of Chemistry, TUM School of Natural Sciences, Technical University of Munich, 85748 Garching, Germany;* orcid.org/0000-0002-1519-5184

Kun-Ting Song − *Physics of Energy Conversion and Storage, Department of Physics, TUM School of Natural Sciences, Technical University of Munich, 85748 Garching, Germany*

Daniel J. Zheng − *Research Laboratory of Electronics, Massachusetts Institute of Technology, Cambridge, Massachusetts 02139, United States;* orcid.org/0000-0002-9471-6856

Max Koch − *Chair of the Synthesis and Characterization of Innovative Materials, TUM School of Natural Sciences, Technical University of Munich, 85748 Garching, Germany;* orcid.org/0000-0003-2275-2337

Ifan E. L. Stephens − *Department of Materials, Imperial College London, London SW7, U.K.*

Shujin Hou − *Chair of Inorganic and Metal−Organic Chemistry, Department of Chemistry, TUM School of Natural Sciences, Technical University of Munich, 85748 Garching, Germany; Physics of Energy Conversion and Storage, Department of Physics, TUM School of Natural Sciences, Technical University of Munich, 85748 Garching, Germany*

Yang Shao-Horn − *Research Laboratory of Electronics, Massachusetts Institute of Technology, Cambridge, Massachusetts 02139, United States;* orcid.org/0000-0001-8714-2121

Complete contact information is available at: https://pubs.acs.org/10.1021/acscatal.4c03618

Notes

The authors declare no competing financial interest.

■ ACKNOWLEDGMENTS

Financial support from DFG project BA 5795/6-1 is gratefully acknowledged. The authors also appreciate the financial support from Deutsche Forschungsgemeinschaft under Germany's excellence strategy EXC 2089/1−390776260, Germany's excellence cluster "e-conversion", and the DFG project MOFMOX (FI 502/43-1). The authors are thankful for the financial support from the TUM network ARTEMIS. X.M. acknowledges the financial support from the China Scholarship Council. The authors thank Suo Tu for their kind help with AFM testing. The authors thank Huifang Fei and Dr. Alberto Varzi for their kind help with XPS testing. Furthermore, the authors gratefully acknowledge the use of the Electron Microscopy Center (EMC) at Rice University.

REFERENCES

(1) Hu, C.; Zhang, L.; Gong, J. Recent progress made in the mechanism comprehension and design of electrocatalysts for alkaline water splitting. *Energy Environ. Sci.* **2019**, *12* (9), 2620−2645.

(2) Ding, J.; Guo, D.; Wang, N.; Wang, H.-F.; Yang, X.; Shen, K.; Chen, L.; Li, Y. Defect Engineered Metal−Organic Framework with Accelerated Structural Transformation for Efficient Oxygen Evolution Reaction. *Angew. Chem., Int. Ed.* **2023**, *62* (43), No. e202311909.

(3) Chu, S.; Majumdar, A. Opportunities and challenges for a sustainable energy future. *Nature* **2012**, *488* (7411), 294−303.

(4) Turner, J. A. Sustainable Hydrogen Production. *Science* **2004**, *305*, 972−974.

(5) Zhao, S.; Tan, C.; He, C.-T.; An, P.; Xie, F.; Jiang, S.; Zhu, Y.; Wu, K.-H.; Zhang, B.; Li, H.; Zhang, J.; Chen, Y.; Liu, S.; Dong, J.; Tang, Z. Structural transformation of highly active metal−organic framework electrocatalysts during the oxygen evolution reaction. *Nature Energy* **2020**, *5* (11), 881−890.

(6) Cheng, W.; Zhao, X.; Su, H.; Tang, F.; Che, W.; Zhang, H.; Liu, Q. Lattice-strained metal−organic-framework arrays for bifunctional oxygen electrocatalysis. *Nature Energy* **2019**, *4* (2), 115−122.

(7) Yuan, S.; Peng, J.; Cai, B.; Huang, Z.; Garcia-Esparza, A. T.; Sokaras, D.; Zhang, Y.; Giordano, L.; Akkiraju, K.; Zhu, Y. G.; Hübner, R.; Zou, X.; Román-Leshkov, Y.; Shao-Horn, Y. Tunable metal hydroxide−organic frameworks for catalysing oxygen evolution. *Nat. Mater.* **2022**, *21* (6), 673−680.

(8) Xue, Z.; Liu, K.; Liu, Q.; Li, Y.; Li, M.; Su, C.-Y.; Ogiwara, N.; Kobayashi, H.; Kitagawa, H.; Liu, M.; Li, G. Missing-linker metal-organic frameworks for oxygen evolution reaction. *Nat. Commun.* **2019**, *10* (1), 5048.

(9) Yang, J.; Shen, Y.; Sun, Y.; Xian, J.; Long, Y.; Li, G. Ir Nanoparticles Anchored on Metal-Organic Frameworks for Efficient Overall Water Splitting under pH-Universal Conditions. *Angew. Chem., Int. Ed.* **2023**, *62* (17), No. e202302220.

(10) Wang, X.; Zhou, W.; Zhai, S.; Chen, X.; Peng, Z.; Liu, Z.; Deng, W.-Q.; Wu, H. Metal-Organic Frameworks: Direct Synthesis by Organic Acid-Etching and Reconstruction Disclosure as Oxygen Evolution Electrocatalysts. *Angew. Chem., Int. Ed.* **2024**, *63* (11), No. e202400323.

(11) Thangasamy, P.; Shanmuganathan, S.; Subramanian, V. A NiCo-MOF nanosheet array based electrocatalyst for the oxygen evolution reaction. *Nanoscale Advances* **2020**, *2* (5), 2073−2079.

(12) Yin, C.; Xu, L.; Pan, Y.; Pan, C. Metal−Organic Framework as Anode Materials for Lithium-Ion Batteries with High Capacity and Rate Performance. *ACS Applied Energy Materials* **2020**, *3* (11), 10776−10786.

(13) Chowdhury, S.; Torad, N. L.; Godara, M.; El-Amir, A. A. M.; Gumilar, G.; Ashok, A.; Rezaul Karim, M.; Abdullah Alnaser, I.; Chaikittisilp, W.; Ray, N.; et al. Hierarchical bimetallic metal-organic frameworks with controllable assembling sub-units and interior architectures for enhanced ammonia detection. *Chemical Engineering Journal* **2024**, *480*, No. 147990.

(14) Fan, Z.-S.; Valentino Kaneti, Y.; Chowdhury, S.; Wang, X.; Karim, M. R.; Alnaser, I. A.; Zhang, F.-B. Weak base-modulated synthesis of bundle-like carbon superstructures from metal-organic framework for high-performance supercapacitors. *Chemical Engineering Journal* **2023**, *462*, No. 142094.

(15) Cheng, P.; Wang, X.; Markus, J.; Abdul Wahab, M.; Chowdhury, S.; Xin, R.; Alshehri, S. M.; Bando, Y.; Yamauchi, Y.; Kaneti, Y. V. Carbon nanotube-decorated hierarchical porous nickel/carbon hybrid derived from nickel-based metal-organic framework for enhanced methyl blue adsorption. *J. Colloid Interface Sci.* **2023**, *638*, 220−230.

(16) Yan, L.; Gopal, A.; Kashif, S.; Hazelton, P.; Lan, M.; Zhang, W.; Chen, X. Metal organic frameworks for antibacterial applications. *Chemical Engineering Journal* **2022**, *435*, No. 134975.

(17) Bennett, T. D.; Coudert, F. X.; James, S. L.; Cooper, A. I. The changing state of porous materials. *Nat. Mater.* **2021**, *20* (9), 1179−1187.

(18) Ehrling, S.; Reynolds, E. M.; Bon, V.; Senkovska, I.; Gorelik, T. E.; Evans, J. D.; Rauche, M.; Mendt, M.; Weiss, M. S.; Poppl, A.; Brunner, E.; Kaiser, U.; Goodwin, A. L.; Kaskel, S. Adaptive response of a metal-organic framework through reversible disorder-disorder transitions. *Nat. Chem.* **2021**, *13* (6), 568−574.

(19) Wu, Y.-P.; Zhou, W.; Zhao, J.; Dong, W.-W.; Lan, Y.-Q.; Li, D.-S.; Sun, C.; Bu, X. Surfactant-Assisted Phase-Selective Synthesis of New Cobalt MOFs and Their Efficient Electrocatalytic Hydrogen Evolution Reaction. *Angew. Chem., Int. Ed.* **2017**, *56* (42), 13001−13005.

(20) Chen, Y.; Liao, P.; Jin, K.; Zheng, Y.; Shao, H.; Li, G. Current progress in metal−organic frameworks and their derivatives for electrocatalytic water splitting. *Inorganic Chemistry Frontiers* **2023**, *10* (22), 6489−6505.

(21) Jia, Y.; Zhang, F.; Liu, Q.; Yang, J.; Xian, J.; Sun, Y.; Li, Y.; Li, G. Single-atomic Fe anchored on hierarchically porous carbon frame for efficient oxygen reduction performance. *Chin. Chem. Lett.* **2022**, *33* (2), 1070−1073.

(22) Zheng, W.; Liu, M.; Lee, L. Y. S. Electrochemical Instability of Metal−Organic Frameworks: In Situ Spectroelectrochemical Investigation of the Real Active Sites. *ACS Catal.* **2020**, *10* (1), 81−92.

(23) Zheng, W.; Lee, L. Y. S. Metal−Organic Frameworks for Electrocatalysis: Catalyst or Precatalyst? *ACS Energy Letters* **2021**, *6* (8), 2838−2843.

(24) Li, F.-L.; Shao, Q.; Huang, X.; Lang, J.-P. Nanoscale Trimetallic Metal-Organic Frameworks Enable Efficient Oxygen Evolution Electrocatalysis. *Angew. Chem., Int. Ed.* **2018**, *57* (7), 1888−1892.

(25) Duan, J.; Chen, S.; Zhao, C. Ultrathin metal-organic framework array for efficient electrocatalytic water splitting. *Nat. Commun.* **2017**, *8* (1), 15341.

(26) Wang, C.-P.; Feng, Y.; Sun, H.; Wang, Y.; Yin, J.; Yao, Z.; Bu, X.-H.; Zhu, J. Self-Optimized Metal−Organic Framework Electrocatalysts with Structural Stability and High Current Tolerance for Water Oxidation. *ACS Catal.* **2021**, *11* (12), 7132−7143.

(27) Li, A.; Kong, S.; Guo, C.; Ooka, H.; Adachi, K.; Hashizume, D.; Jiang, Q.; Han, H.; Xiao, J.; Nakamura, R. Enhancing the stability of cobalt spinel oxide towards sustainable oxygen evolution in acid. *Nature Catalysis* **2022**, *5* (2), 109−118.

(28) Lin, C.; Li, J.-L.; Li, X.; Yang, S.; Luo, W.; Zhang, Y.; Kim, S.-H.; Kim, D.-H.; Shinde, S. S.; Li, Y.-F.; Liu, Z.-P.; Jiang, Z.; Lee, J.-H. In-situ reconstructed Ru atom array on α-MnO2 with enhanced performance for acidic water oxidation. *Nature Catalysis* **2021**, *4* (12), 1012−1023.

(29) Klaus, S.; Cai, Y.; Louie, M. W.; Trotochaud, L.; Bell, A. T. Effects of Fe Electrolyte Impurities on Ni(OH)2/NiOOH Structure and Oxygen Evolution Activity. *J. Phys. Chem. C* **2015**, *119* (13), 7243−7254.

(30) Lee, S.-Y.; Kim, I.-S.; Cho, H.-S.; Kim, C.-H.; Lee, Y.-K. Resolving Potential-Dependent Degradation of Electrodeposited Ni(OH)2 Catalysts in Alkaline Oxygen Evolution Reaction (OER): In Situ XANES Studies. *Applied Catalysis B: Environmental* **2021**, *284*, No. 119729.

(31) Ma, X.; Zheng, D. J.; Hou, S.; Mukherjee, S.; Khare, R.; Gao, G.; Ai, Q.; Garlyyev, B.; Li, W.; Koch, M.; Mink, J.; Shao-Horn, Y.; Warnan, J.; Bandarenka, A. S.; Fischer, R. A. Structure−Activity Relationships in Ni- Carboxylate-Type Metal−Organic Frameworks' Metamorphosis for the Oxygen Evolution Reaction. *ACS Catal.* **2023**, *13* (11), 7587−7596.

(32) Choi, A.; Kim, Y. K.; Kim, T. K.; Kwon, M.-S.; Lee, K. T.; Moon, H. R. 4,4′-Biphenyldicarboxylate sodium coordination compounds as anodes for Na-ion batteries. *J. Mater. Chem. A* **2014**, *2* (36), 14986−14993.

(33) Böhm, D.; Beetz, M.; Kutz, C.; Zhang, S.; Scheu, C.; Bein, T.; Fattakhova-Rohlfing, D. V(III)-Doped Nickel Oxide-Based Nanocatalysts for Electrochemical Water Splitting: Influence of Phase, Composition, and Doping on the Electrocatalytic Activity. *Chem. Mater.* **2020**, *32* (24), 10394−10406.

(34) Hall, D. S.; Lockwood, D. J.; Poirier, S.; Bock, C.; MacDougall, B. R. Raman and Infrared Spectroscopy of α and β Phases of Thin

https://doi.org/10.1021/acscatal.4c03618
ACS Catal. 2024, 14, 15916−15926

Nickel Hydroxide Films Electrochemically Formed on Nickel. *J. Phys. Chem. A* **2012**, *116* (25), 6771−6784.
(35) Butova, V. V.; Budnyk, A. P.; Charykov, K. M.; Vetlitsyna-Novikova, K. S.; Bugaev, A. L.; Guda, A. A.; Damin, A.; Chavan, S. M.; Øien-Ødegaard, S.; Lillerud, K. P.; Soldatov, A. V.; Lamberti, C. Partial and Complete Substitution of the 1,4-Benzenedicarboxylate Linker in UiO-66 with 1,4-Naphthalenedicarboxylate: Synthesis, Characterization, and H2-Adsorption Properties. *Inorg. Chem.* **2019**, *58* (2), 1607−1620.
(36) Aufa, M. H.; Watzele, S. A.; Hou, S.; Haid, R. W.; Kluge, R. M.; Bandarenka, A. S.; Garlyyev, B. Fast and accurate determination of the electroactive surface area of MnOx. *Electrochim. Acta* **2021**, *389*, No. 138692.
(37) Hou, S.; Xu, L.; Mukherjee, S.; Zhou, J.; Song, K.-T.; Zhou, Z.; Zhang, S.; Ma, X.; Warnan, J.; Bandarenka, A. S.; Fischer, R. A. Impact of Organic Anions on Metal Hydroxide Oxygen Evolution Catalysts. *ACS Catal.* **2024**, *14* (16), 12074−12081.
(38) Qiu, Y.; Lopez-Ruiz, J. A.; Sanyal, U.; Andrews, E.; Gutiérrez, O. Y.; Holladay, J. D. Anodic electrocatalytic conversion of carboxylic acids on thin films of RuO2, IrO2, and Pt. *Applied Catalysis B: Environmental* **2020**, *277*, No. 119277.
(39) Qiu, Y.; Lopez-Ruiz, J. A.; Zhu, G.; Engelhard, M. H.; Gutiérrez, O. Y.; Holladay, J. D. Electrocatalytic decarboxylation of carboxylic acids over RuO2 and Pt nanoparticles. *Applied Catalysis B: Environmental* **2022**, *305*, No. 121060.
(40) Farhat, R.; Dhainy, J.; Halaoui, L. I. OER Catalysis at Activated and Codeposited NiFe-Oxo/Hydroxide Thin Films Is Due to Postdeposition Surface-Fe and Is Not Sustainable without Fe in Solution. *ACS Catal.* **2020**, *10* (1), 20−35.
(41) Qian, Q.; Li, Y.; Liu, Y.; Yu, L.; Zhang, G. Ambient Fast Synthesis and Active Sites Deciphering of Hierarchical Foam-Like Trimetal−Organic Framework Nanostructures as a Platform for Highly Efficient Oxygen Evolution Electrocatalysis. *Adv. Mater.* **2019**, *31* (23), No. 1901139.
(42) Hou, S.; Li, W.; Watzele, S.; Kluge, R. M.; Xue, S.; Yin, S.; Jiang, X.; Döblinger, M.; Welle, A.; Garlyyev, B.; Koch, M.; Müller-Buschbaum, P.; Wöll, C.; Bandarenka, A. S.; Fischer, R. A. Metamorphosis of Heterostructured Surface-Mounted Metal−Organic Frameworks Yielding Record Oxygen Evolution Mass Activities. *Adv. Mater.* **2021**, *33* (38), No. 2103218.
(43) Zheng, D. J.; Görlin, M.; McCormack, K.; Kim, J.; Peng, J.; Xu, H.; Ma, X.; LeBeau, J. M.; Fischer, R. A.; Román-Leshkov, Y.; Shao-Horn, Y. Linker-Dependent Stability of Metal-Hydroxide Organic Frameworks for Oxygen Evolution. *Chem. Mater.* **2023**, *35* (13), 5017−5031.
(44) Eom, S. Y.; Lee, Y. R.; Kwon, C. H.; Kim, H. L. Surface enhanced Raman scattering of 2,2′-biphenyl dicarboxylic acid on silver surfaces: Structure and orientation upon adsorption. *J. Mol. Struct.* **2016**, *1115*, 70−74.
(45) Lee, S.; Banjac, K.; Lingenfelder, M.; Hu, X. Oxygen Isotope Labeling Experiments Reveal Different Reaction Sites for the Oxygen Evolution Reaction on Nickel and Nickel Iron Oxides. *Angew. Chem., Int. Ed.* **2019**, *58* (30), 10295−10299.
(46) Kostecki, R.; McLarnon, F. Electrochemical and In Situ Raman Spectroscopic Characterization of Nickel Hydroxide Electrodes. *J. Electrochem. Soc.* **1997**, *144*, 485.
(47) Han, Y.; Liu, Z. H.; Yang, Z.; Wang, Z.; Tang, X.; Wang, T.; Fan, L.; Ooi, K. Preparation of Ni^{2+}-Fe^{3+} Layered Double Hydroxide Material with High Crystallinity and Well-Defined Hexagonal Shapes. *Chem. Mater.* **2008**, *20*, 360−363.
(48) Qiu, Z.; Tai, C.-W.; Niklasson, G. A.; Edvinsson, T. Direct observation of active catalyst surface phases and the effect of dynamic self-optimization in NiFe-layered double hydroxides for alkaline water splitting. *Energy Environ. Sci.* **2019**, *12* (2), 572−581.
(49) Rui, K.; Zhao, G.; Chen, Y.; Lin, Y.; Zhou, Q.; Chen, J.; Zhu, J.; Sun, W.; Huang, W.; Dou, S. X. Hybrid 2D Dual-Metal-Organic Frameworks for Enhanced Water Oxidation Catalysis. *Adv. Funct. Mater.* **2018**, *28* (26), No. 1801554.

https://doi.org/10.1021/acscatal.4c03618
ACS Catal. 2024, 14, 15916−15926